COMMUNICATIONS CHEMISTRY

ARTICLE

https://doi.org/10.1038/s42004-018-0104-1 OPEN

# Atomistics of pre-nucleation layering of liquid metals at the interface with poor nucleants

Sida Ma[1,2], Adam J. Brown[3,7], Rui Yan[1], Ruslan L. Davidchack[2], Paul B. Howes[4], Chris Nicklin[5], Qijie Zhai[6], Tao Jing[1] & Hongbiao Dong[3]

Liquid layering at heterogeneous solid/liquid interfaces is a general phenomenon, which provides structural templates for nucleation of crystalline phases on potent nucleants. However, its efficacy near poor nucleants is incompletely understood. Here we use a combination of X-ray crystal truncation rod analysis and ab initio molecular dynamics to probe the pre-nucleation liquid layering at the sapphire–aluminium solid/liquid interface. At the sapphire side, a ~1.6 aluminium-terminated structure develops, and at the liquid side, two pre-nucleation layers emerge at 950 K. No more pre-nucleation layer forms with decreasing temperature indicating that nucleation of crystalline aluminium through layer-by-layer atomic adsorption of liquid atoms is not favoured. Instead, the appearance of stochastically-formed nuclei near the substrate is supported by our experiments. Nucleation on poor nucleants is dominated by the stochastic nucleation events which are substantially influenced by the pre-nucleation layers that determine the surface structure in contact with the nuclei.

[1] School of Materials Science and Engineering, Tsinghua University, 100084 Beijing, China. [2] Department of Mathematics, University of Leicester, Leicester LE1 7RH, UK. [3] Department of Engineering, University of Leicester, Leicester LE1 7RH, UK. [4] Department of Physics, University of Leicester, Leicester LE1 7RH, UK. [5] Diamond Light Source Harwell Science and Innovation Campus, Harwell OX11 0DE, UK. [6] State Key Laboratory of Advanced Special Steels, Shanghai University, 200072 Shanghai, China. [7] Present address: The Manufacturing Technology Centre Ansty Park, Coventry, CV7 9JU, UK. Correspondence and requests for materials should be addressed to H.D. (email: h.dong@le.ac.uk)

In Classical Nucleation Theory (CNT), nucleation of a crystalline phase is believed to originate from the stochastically formed nuclei[1] (~10–1000 atoms[2]) driven by energy fluctuations. Such nuclei may manifest as spherical caps when forming on foreign surfaces, which is termed as heterogeneous nucleation. Recently, this theory has been challenged by the observation of pre-nucleation layers (PNLs) adjacent to the atomically smooth solid surfaces[3–10]. Different from the nuclei described by the CNT, the PNLs are thermodynamically stable structures that normally appear at a temperature above the liquids ($T_1$) by spontaneous liquid layering, and the formation of the PNLs is believed to be an adsorption process. When the temperature falls below $T_1$, it is reasonable to predict that the liquid layering may continue and compete with the energy fluctuations to govern heterogeneous nucleation behaviours. If the liquid layering dominates, heterogeneous nucleation of the crystalline phase proceeds layer-by-layer through a structural templating process; if the energy fluctuations dominate, stochastically formed atomic clusters may become the nuclei and heterogeneous nucleation obey the rules described by the CNT.

The significant role played by the PNLs in influencing heterogeneous nucleation of the crystalline phase has been well explained for systems with potent nucleant substrates, such as liquid Al with Al–Ti–B inoculation[11–14]. At the atomic scale, the nuclei formed on potent nucleant substrates (contact angle $\theta < 20°$) are predicted to be only several atoms thick[15], which can be approximated as two-dimensional (2D) layered structures. If PNLs appear in the vicinity of the substrates, they will readily transform into the 2D crystal nuclei when the temperature falls below $T_1$. These 2D nuclei trigger heterogeneous nucleation and then grow in a manner described by the free-growth model[11]. Hence, heterogeneous nucleation of the crystalline phase on the potent nucleant substrates is most likely to be dominated by the liquid layering, which causes the formation of the PNLs.

On the contrary, for systems with poor nucleant substrates ($\theta > 40°$), the critical nucleus size is large enough for the contact angle to be well defined. Therefore, the nuclei manifest as three-dimensional (3D) atomic clusters, which are different from the structures of the PNLs. However, it is worth noting that the poor nucleant substrates normally have large lattice mismatches with the crystals[16,17], and the PNLs can act as a transition structure to accommodate the substantial structural differences across the interface thus reducing the energy barrier for heterogeneous nucleation. As such, both the CNT-based 3D atomic clusters and the 2D crystal embryo evolved from the PNLs could be the initial nucleus structures. Therefore, it is desirable and imperative to have a further understanding of the heterogeneous nucleation mechanism of the crystalline phase on a poor nucleant substrate. Sapphire ($\alpha$-$Al_2O_3$) substrate is a typical poor nucleant substrate for liquid Al[18]. However, only a limited number of studies[4,7,19–24] exist regarding the sapphire–Al solid/liquid (S/L) interface. Zhang et al.[21] first predicted the presence of the PNLs at the (0001) sapphire–Al S/L interface using the reactive force field. This prediction has been confirmed by the direct experimental observation by Oh et al.[4] using high-resolution transmission electron microscopy (HRTEM). However, these studies obtained different atomic configurations for the outermost layer of sapphire. Zhang et al.[21] observed an Al–O mixed configuration; Oh et al.[4] obtained an O-rich structure; while Kang et al.[20], using ab initio molecular dynamics (AIMD), obtained an Al-rich configuration. The inconsistency in the atomic arrangement at this interface has not been clearly explained because of the difficulty in the atomic-scale characterisation of the S/L interface both theoretically and experimentally. As an interface-sensitive, angstrom-scale resolution surface X-ray diffraction (SXRD) and X-ray crystal truncation rod (CTR) analysis has provided new insights into atomic arrangements at surfaces and interfaces[6,25–33]. Compared with HRTEM, the CTR technique is a spatially averaged (~$0.2 \times 0.25$ $mm^2$ in our experiment) method that can also easily distinguish the atomic species[34]. Recently, Schülli et al.[6] and Vonk et al.[30] have explored the CTR technique in characterising the structural features of the S/L interface, which confirmed the capability of the CTR technique in characterising the S/L interface.

Here the atomistics of the pre-nucleation liquid layering at the (0001) sapphire–Al S/L interface is explored through the combination of the CTR measurement and complementary AIMD simulations. Here we show that, when liquid Al is brought into contact with (0001) sapphire surface at 950 K, liquid layering occurs leading to the formation of two PNLs at the interface. Meanwhile, the sapphire surface transforms into a ~1.6 Al-terminated structure. Kinetic analysis indicates that the pre-nucleation liquid layering can be described as layer-by-layer adsorption of liquid atoms onto the substrate. However, further adsorption of liquid atoms onto the existing PNLs (even when the temperature is much lower than $T_1$) is difficult, which impedes the propagation of liquid layering into the bulk liquid. We propose that 3D nuclei may form stochastically near the surface of the existing PNLs and then dominate the nucleation of crystalline Al, which is supported by the in situ XRD and CTR experimental results.

## Results

**Atomic-scale visualisation of PNLs**. In this work, the Miller indices (*HKL*), defining the reciprocal space of the sapphire substrate, are used to describe a CTR. The (01*L*) CTR curves measured, respectively, from the (0001) sapphire surface, the (0001) sapphire–Al S/S interface (Al deposited by the magnetron sputtering) and the (0001) sapphire–Al S/L interface (at around 950 K) are depicted in Fig. 1. There is virtually no distinguishable difference in the CTR curves measured at the sapphire surface and the sapphire–Al S/S interface, while the difference between the S/S and S/L interfaces is evident, particularly at $L = 3$–5. The intensity peak at $L = 3$–5 in the CTR curve measured at the S/L interface could be attributed to the presence of the PNLs. To verify this, and to construct the sapphire–Al S/L interface model, we employ a two-step fitting approach to link the CTR curves to the interfacial atomic arrangement. In the first fitting step, CTR curves are fitted to several (0001) sapphire surface models. As shown in Fig. 2, four initial fitting models are used in the first fitting step. These four models have different (0001) sapphire surface terminations: (1) the stoichiometric termination (1Al), (2) the Al-rich termination (2Al), (3) the fully hydroxylated termination (3OH), and (4) the partly hydroxylated termination (1Al+1OH). These terminations are all likely to exist under our experimental conditions[35,36]. According to Eng at al.'s[28] experimental study, the (0001) sapphire surface is readily hydroxylated by the dissociation of water molecules, and water vapour pressure of 1 torr is sufficient to fully hydroxylate this surface. In our experiments, the (0001) sapphire surface samples were stored in the open air before the deposition of pure aluminium. Thus it is reasonable to infer that surface hydroxylation occurred before the magnetron sputtering was conducted to obtain the (0001) sapphire–Al interface samples. This is why the fully and partly hydroxylated (0001) sapphire surface models were considered in the first fitting step. Although we demonstrate that the existence of hydroxyls at the (0001) sapphire–liquid Al interface is not favoured by the fit, considering the hydroxylated (0001) sapphire surface models in the first fitting step was necessary to make the fitting results more comprehensive. Note that all the hydrogen atoms in the fitting models are omitted because of the difficulty of detecting them in the SXRD experiments[28]. Therefore, the fully

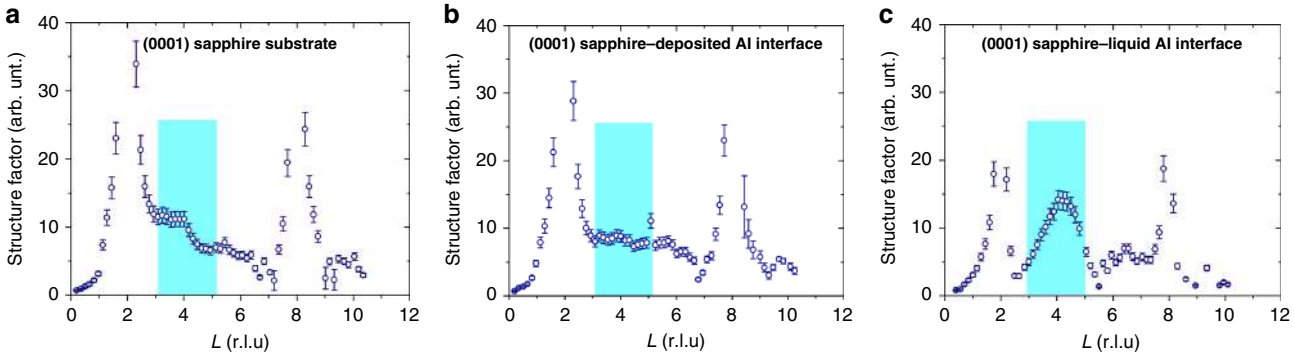


**Fig. 1** Comparison among the (01*L*) CTR curves of different samples. **a** (01*L*) CTR curve measured at the (0001) sapphire surface. **b** (01*L*) CTR curve collected at the (0001) sapphire–solid Al interface. Solid Al is deposited onto the (0001) sapphire surface using magnetron sputtering during which high-purity Ar was used as the sputtering gas under a working pressure of $1 \times 10^{-2}$ mbar and a high-purity (99.9999%) Al target was operated at 120 W. **c** (01*L*) CTR curve of the (0001) sapphire–liquid Al interface measured at around 950 K, which was obtained by melting the (0001) sapphire–solid Al interface. The cyan highlighted regions depict the differences among these three CTR curves, and it is proposed in this work that the intensity peak at $L = 3$–5 in **c** is attributed to the formation of the PNLs. The error bars in all these three panels are derived from the statistical uncertainty of the measured intensity and are set to 10% of the structure factor value whenever it is <10%, which is an estimate of the systematic error

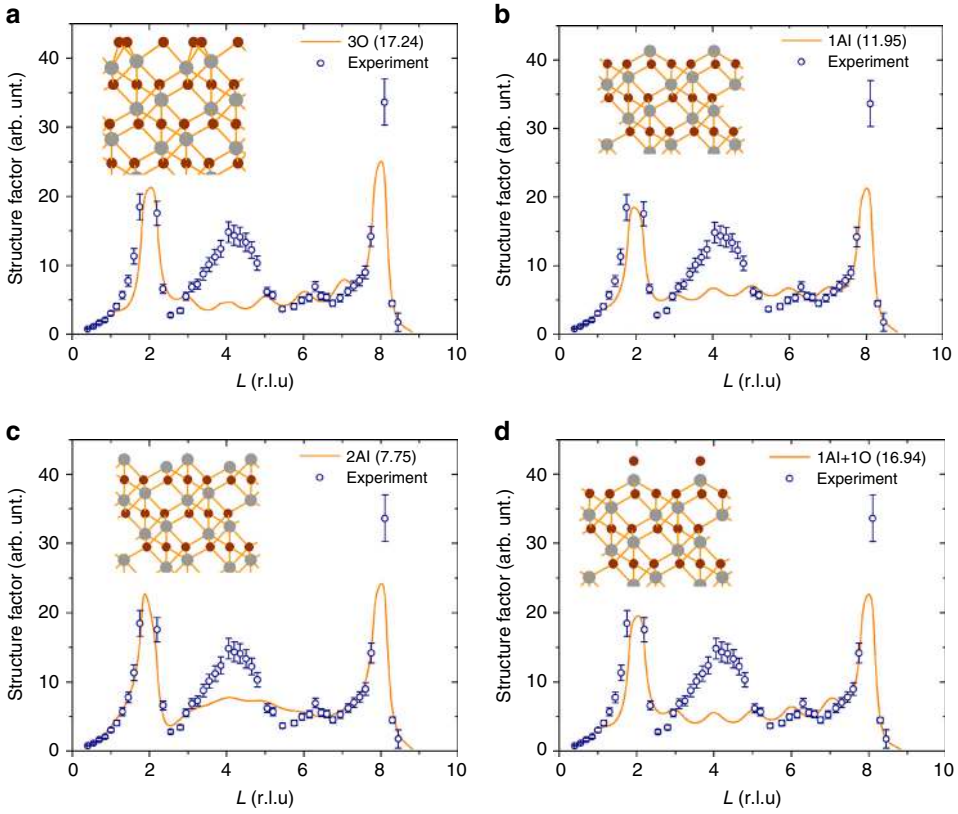


**Fig. 2** Fitting of the (01*L*) CTR data to different surface models in the first fitting step. **a**–**d** Four (0001) sapphire surface models (inset in each panel, grey circles denote Al atoms and brown circles denote O atoms) and the corresponding fitting results using the (01*L*) CTR curve measured at the sapphire–liquid Al interface under 950 K. The goodness of fitting (normalised $\chi^2$) of each model is shown in parentheses. The error bars in all these four panels estimate the statistical and systematic errors of the measured structure factor data in the (01*L*) CTR curve. The approach to obtain the error bars is explained in the Methods section. It is obviously observed that the 2Al-terminated surface (**c**) is the best-fit surface model among these four models. However, it is also worth noting that large deviations at $L = 3$–5 between the experimental and fitted CTR curves still exists even for the best-fit surface model (**c**). This implies that there exist other structures (such as the PNLs) at this interface that contribute to the intensity peak of the CTR curve at $L = 3$–5

and partly hydroxylated (0001) sapphire surface models can be treated as 3O (Fig. 2a) and 1Al+1O (Fig. 2d) terminations, respectively. Results of fitting the CTR data to the above surface models show that the 2Al model (Fig. 2c) gives rise to the best fit among the four models.

The above analysis shows that after interaction with the liquid Al the (0001) sapphire surface evolves into an Al-rich termination; however, significant deviation between the theoretical and experimental CTR curves still exists (particularly at $L = 3$–5), even for the best-fit 2Al model. This deviation cannot be attributable to the disordered bulk liquid Al atoms, which

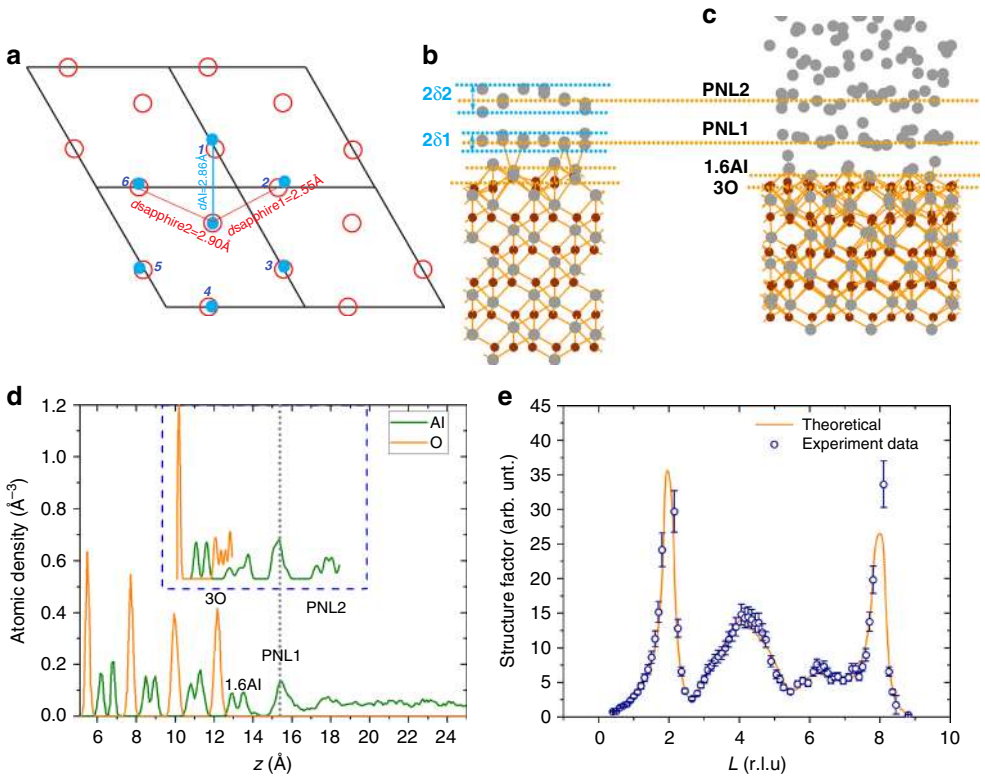


**Fig. 3** (0001) sapphire–liquid Al interfacial structure obtained from the CTR measurement and AIMD simulations. **a** Sapphire (0001)//Al (111) orientation relationship. Oxygen atoms in the 3O layer are displayed by the hollow red circles, and the solid blue circles indicate seven nearest-neighbour atoms on the Al (111) plane. The 1.6 Al layer is omitted for clarity. Two different types of interfacial lattice mismatches arise for the fully coherent interface: $f_1 = -10.75\%$ (corresponds to oxygen 1 and 2, with interatomic distance $d_{\text{sapphire1}} = 2.55$ Å) and $f_2 = 1.4\%$ (corresponds to oxygen 3, 4, 5, and 6, with $d_{\text{sapphire2}} = 2.90$ Å). Interfacial lattice mismatch is calculated according to $f = (d_{\text{sapphire}} - d_{\text{Al}})/(d_{\text{Al}})$, so negative $f$ means a compressive stress state in the aluminium, whereas positive $f$ means a tensile stress state. **b**, **c** Side view of the (0001) sapphire–liquid Al interfacial structure obtained from the CTR and the AIMD, respectively. The small brown circles are O atoms, and the large grey circles are Al atoms. Only the two PNLs of liquid Al are shown in the CTR-based structure. The horizontal orange lines that cross **b**, **c** depict four atomic layers (3O layer, 1.6 Al layer, PNL1 and PNL2, respectively) in the interface models. The horizontal blue lines in **b** explain the layer amplitudes of the PNL1 and PNL2 ($\delta_1$ and $\delta_2$, which are the half of the widths depicted by the double-headed arrows), respectively, whose values are listed in Table 1. **d** Atomic density profiles along the $z$-direction (the direction perpendicular to the interface) for the interfacial structure obtained from the AIMD simulation and the CTR fitting (shown in the inset of **d**). The peak positions of the PNL1 for these two profiles are aligned with each other, as shown by the grey dotted vertical line in **d**. **e** CTR fitting result with normalised $\chi^2 \approx 1.9$, which shows that the theoretical model used in the fitting coincides well with the experimental result. The error bars in **e** show the statistical and systematic errors of the measured structure factor data in the (01$L$) CTR curve. The approach to obtain the error bars is explained in the Methods section

contribute only to background noise. Thus the presence of PNLs, which are partially ordered structures, is likely the principal reason causing the deviations. In the second step, several PNLs are added to the 2Al sapphire surface model. The PNLs are modelled as several close-packed layers, which are coherently combined with the sapphire substrate using the widely accepted orientation relationship (OR)[37]: sapphire $(0001)[10\bar{1}0] \parallel$ Al $(111)[1\bar{1}0]$ (Fig. 3a). During the fitting, all the atoms in the initial models are allowed to move independently along the direction perpendicular to the interface. When dealing with the in-plane atomic arrangement, each PNL is treated as a rigid body rather than several independently moving atoms. The atomic occupancies and the in-plane Debye–Waller (DW) parameters are applied to quantify the degree of in-plane ordering of the PNLs. Fitting results of the second fitting step depicted in Fig. 3e show that addition of PNLs nearly eliminates the differences between the theoretical and experimental CTR curves. Additionally, the results illustrate that the intensity peak at $L = 3$–$5$ of the CTR curves measured at the sapphire–Al S/L interface is attributable to the PNLs. The layer number of the PNLs is determined to be two, as adding three or more layers does not give rise to further improvement of the goodness of fit (Supplementary Figure 1).

Except for the (01$L$) CTR, five other CTR curves ((10$L$), (11$L$), (20$L$), $(\bar{2}1L)$, and $(1\bar{2}L)$) have also been fitted using the fitting steps introduced above. It is found that better fitting accuracy can be obtained when the double-layer PNLs are included in the initial fitting model compared with the model without the PNLs (Supplementary Figure 2), which confirms the existence of the PNLs at this interface. Table 1 shows the fitting results based on the six CTR curves, from which we find that the parameter values obtained from all the six CTR curves are close to each other.

The sapphire–PNLs interfacial structure obtained from the (01$L$) CTR fitting is shown in Fig. 3b. The double-layer PNLs are buckled with atoms diffusing in the $z$-direction (the direction perpendicular to the interface), indicating that the PNLs are not fully ordered layers. To quantify the degree of out-of-plane ordering of the PNLs, the layer amplitude $\delta_i$ (standard deviation of the $z$-coordinates of the atoms within the layer, $i$ represents the index of a PNL layer) is calculated for each PNL and listed in Table 1. The values of $\delta_i$ suggest that the first PNL (PNL1) has a much higher degree of out-of-plane ordering than the second PNL (PNL2). This trend is also reflected by the out-of-plane DW

**Table 1 Values of the main parameters from the CTR data fitted to the double-layer PNL model**

| Parameters | (01*L*) CTR | (10*L*) CTR | (20*L*) CTR | ($\bar{2}$1*L*) CTR | (11*L*) CTR | (1$\bar{2}$*L*) CTR |
|---|---|---|---|---|---|---|
| Surface roughness parameter, $\beta$ | 0.040 ± 0.006 | 0.035 ± 0.006 | 0.035 ± 0.009 | 0.045 ± 0.007 | 0.039 ± 0.007 | 0.039 ± 0.006 |
| Liquid fraction, $f_\alpha$ | 99.4% ± 0.6% | 98% ± 2% | 99% ± 3% | 98% ± 1% | 98% ± 2% | 98% ± 1% |
| Interlayer distance (PNL1–1.6 Al) | 1.90 ± 0.03 Å (2.19 Å[a] 3.5 ± 0.25 Å[b]) | 1.79 ± 0.01 Å | 1.75 ± 0.07 Å | 1.8 ± 0.1 Å | 1.8 ± 0.1 Å | 1.92 ± 0.06 Å |
| Interlayer distance (PNL2–PNL1) | 2.84 ± 0.03 Å (2.30 Å[a] 2.85 ± 0.25 Å[b]) | 2.78 ± 0.07 Å | 2.9 ± 0.1 Å | 2.8 ± 0.1 Å | 2.9 ± 0.2 Å | 2.8 ± 0.1 Å |
| $\delta_1$ | 0.018 Å | 0.023 Å | 0.019 Å | 0.011 Å | 0.021 Å | 0.015 Å |
| $\delta_2$ | 0.042 Å | 0.046 Å | 0.039 Å | 0.037 Å | 0.036 Å | 0.050 Å |
| $D_i^{\perp}$ | | | | | | |
| PNL1 | 1.3 ± 0.7 | 1.0 ± 0.2 | 1.0 ± 0.9 | 1.0 ± 0.8 | 1.0 ± 0.4 | 1.0 ± 0.6 |
| PNL2 | 15.8 ± 0.4 | 14.0 ± 0.5 | 14.0 ± 2.2 | 14 ± 9 | 14 ± 2 | 14 ± 2 |
| $D_i^{//}$ | | | | | | |
| PNL1 | 1.5 ± 0.6 | 1 ± 1 | 1.8 ± 0.8 | 1.9 ± 0.5 | 1.6 ± 0.5 | 1.5 ± 0.6 |
| PNL2 | 11 ± 2 | 10 ± 1 | 10.1 ± 0.8 | 10 ± 3 | 11.5 ± 0.7 | 10.6 ± 0.7 |

The liquid fraction parameter $f_\alpha$ is used to estimate the coverage of the PNL structure on top of the substrate surface. All the other parameters have been introduced in the context
[a]AIMD results in this work
[b]Result from Oh et al.[4]

parameters ($D_i^{\perp}$), which characterise temperature influence on the XRD intensity and also quantify the degree of ordering[38]. From Table 1, we find $D_2^{\perp} >> D_1^{\perp} > 0$, indicating that PNL2 contributes much less to the diffraction intensity than PNL1, which is further evidence of the attenuation of the degree of out-of-plane ordering with increasing distance from the substrate. The interfacial structure obtained from the CTR experiments is compared with the AIMD results, as shown in Fig. 3. Both experiments and simulations show a double-layer PNL structure near the (0001) sapphire substrate, with PNL2 being much less ordered than PNL1, which confirms the ability of the AIMD method to faithfully reproduce the PNLs at the S/L interfaces. The observation of double-layer PNLs in this work is similar to the experimental findings of Oh et al.[4] except for the interlayer distance from PNL1 to the outermost layer of the sapphire substrate, which is 1.90 ± 0.03 Å in this work compared with a larger value (3.5 ± 0.25 Å) in Oh's HRTEM results. This difference may arise from the 1.6 Al layer (as shown in Fig. 3), which is the outermost layer of the (0001) sapphire substrate in our experiments and simulations, but is absent in Oh's results. In the fitted interfacial structure (Fig. 3b), the layer-averaged atomic occupancy ($O_c$) of the 1.6 Al layer is 81 ± 1% (corresponds to an average of 1.6 Al atoms), which is consistent with the AIMD result ($O_c \approx 83.3\%$, shown in Fig. 4a).

In-plane features of the PNLs are characterised by the in-plane DW ($D_i^{//}$) and $O_c$. From Table 1, it is found that $D_2^{//} >> D_1^{//} > 0$, meaning the decay in the degree of in-plane ordering of the PNLs with distance to the interface increasing. $O_c$ of PNL1 is determined to be 82% ± 3% (relative to a close-packed atomic layer) by fitting the (01*L*) CTR curve to the interface model. In AIMD simulations, the in-plane structure of the PNL1 is analysed at different temperatures (Fig. 4b). It is expected that decreasing temperature will increase the degree of in-plane ordering, which is illustrated in Fig. 4b by the orientational order parameter[39] $q_6$ and in-plane coordination number $N_{in}$ of the PNL1. $q_6$ increases from around 0.2 to approximately 0.45 as temperature decreases indicating that the six-fold symmetry of the PNL1 is significantly enhanced by the reduction of system temperature. This trend is also reflected by the 2D structural factor distributions in Fig. 4. The above analysis implies that the PNL1 has the tendency of becoming a close-packed layer with temperature decreasing; however, it is worth noting that $q_6$ is still substantially smaller than 1.0, which is the $q_6$ value for an atomic layer with a perfect six-fold symmetry. Additionally, $N_{in}$ of PNL1 (Fig. 4b) is evidently <6.0 ($N_{in}$ for a close-packed atomic layer) even at a temperature (such as 700 K) much lower than the Al melting point (around 933 K). This indicates that a large energy barrier exists that prevents the PNL1 from becoming an ordered and close-packed layer.

One impediment for the PNL1 to becoming ordered is the interfacial lattice mismatch $f$ between the (0001) sapphire surface and PNL1. We analyse the theoretical $f$ between the (0001) sapphire surface and an Al (111) layer with Al atoms in the Al (111) layer fully coherent with the underlying (0001) sapphire surface, as shown in Fig. 3a. Interfacial lattice mismatch $f$ is calculated according to the following formula, $f = (d_{sapphire} - d_{Al})/(d_{Al})$, where $d_{sapphire}$ and $d_{Al}$ are the interatomic distances at the sapphire (0001) plane and the Al (111) plane, respectively, as illustrated in Fig. 3a. Two sets of interfacial lattice mismatches, $f_1 = -10.75\%$ and $f_2 = 1.4\%$, arise at this interface, among which the large negative mismatch $f_1$ will induce enormous in-plane compressive stress within the Al layers. Compared with the in-plane tensile stress that is beneficial to the accumulation of atoms, the in-plane compressive stress drives the atoms out of each layer, resulting in the atomic density depletion near the interface. Hence, the PNLs near the (0001) sapphire substrate endure tremendous resistance to becoming denser. According to the studies of Alert et al.[20,40] and Duan et al.[9], atomic density plays a pivotal role in the formation of liquid layers. Therefore, the low atomic density of PNLs near the (0001) sapphire substrate caused by the large negative interfacial lattice mismatch hinders the further ordering of the PNL1.

In summary, a double-layer PNL structure is observed adjacent to the ~1.6 Al-terminated (0001) sapphire–Al S/L interface. The degree of the out-of-plane ordering of PNL1 is relatively high, while its in-plane structure is poorly ordered even at the undercooled liquid with a large undercooling. Additionally, the degree of ordering (both out-of-plane and in-plane) decays rapidly as the distance to the sapphire substrate increases.

**Kinetics of pre-nucleation liquid layering**. In this section, the formation kinetics of the 1.6 Al layer and PNLs at 950 K are analysed using the AIMD simulations. As depicted in Fig. 5a, the (0001) sapphire–liquid Al interface undergoes drastic modification within the first 1.0 ps, during which the main features of the 1.6 Al layer and PNLs develop. Then as the S/L interfacial

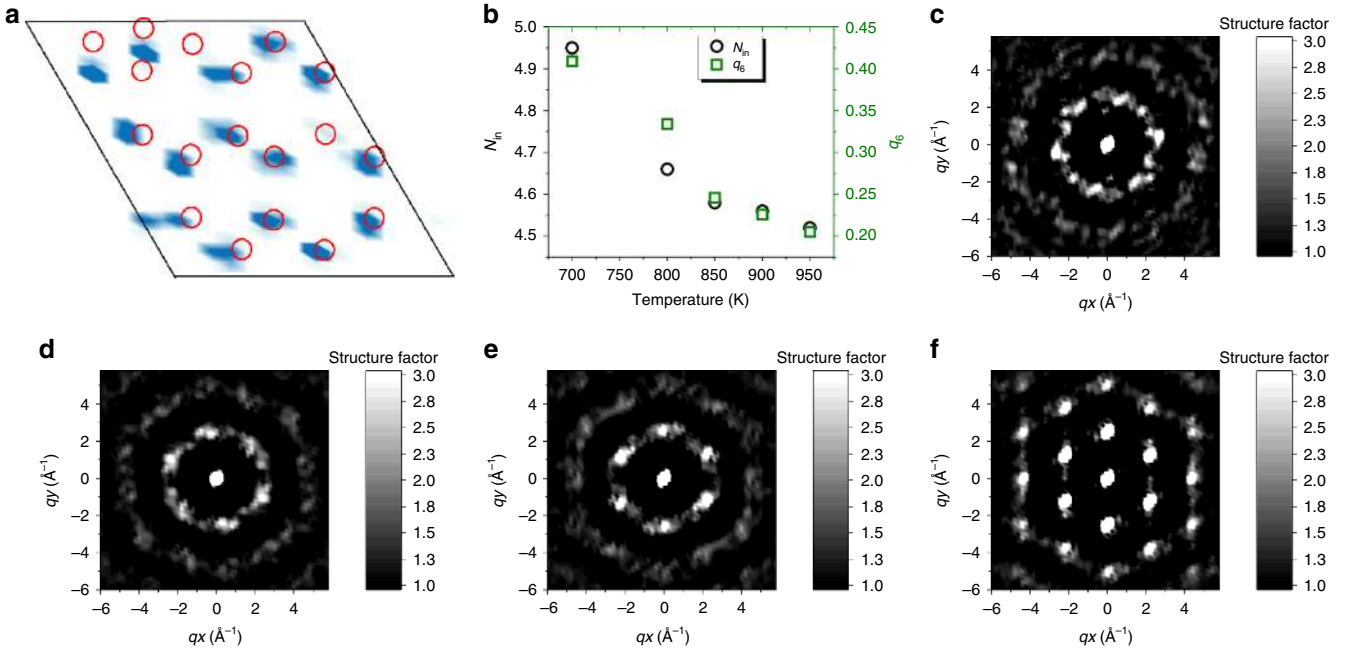


**Fig. 4** In-plane structures of the 1.6 Al layer and the PNLs. **a** Comparison between the 1.6 Al layer in-plane atomic density (blue spots) and the in-plane atomic arrangement of the 2 Al layer (hollow red circles) at the 2 Al terminated (0001) sapphire surface. From this panel, it is observed that Al atoms in the 1.6 Al layer occupy approximately 83.3% of the Al atomic sites in the 2 Al layer. **b** Influence of system temperature on in-plane coordination number $N_{in}$ and orientational order parameter $q_6$. These parameters are calculated within the PNL1 using the AIMD trajectories from 45.0 to 50.0 ps under each temperature, respectively. For a perfectly ordered close-packed layer, $N_{in} = 6$ and $q_6 = 1$. **c**–**f** Two-dimensional structure factor distributions of the PNL1 at 950, 900, 850 and 700 K, respectively, which are computed using the AIMD trajectories from 45.0 to 50.0 ps. *qx* and *qy* are respectively, the *x*- and *y*-components of the scattering vector **q** in the reciprocal space

interaction continues, the atomic density peaks corresponding to the 1.6 Al layer and PNL1 sharpen (Fig. 5a), indicating an increase in the degree of out-of-plane ordering for these two layers. This simultaneous ordering of the 1.6 Al layer and the PNL1 implies that their formation kinetics are inter-related. To have a further look at the formation kinetics of the 1.6 Al layer and PNLs, the (0001) sapphire–liquid Al interfacial force profile (Fig. 5b) and the (0001) sapphire surface force profile (Fig. 5c) are computed along the *z*-direction, respectively. To obtain the interfacial force profile, the *z*-components of the forces imposed on each Al atom $F_z$(A1) are recorded and averaged during 0–1.0 ps. Figure 5b shows the interfacial force profile, from which we can correctly predict the positions of the 1.6 Al layer and the two PNLs (depicted by the horizontal dotted blue lines). This suggests that the pre-nucleation liquid layering is a spontaneous and deterministic process driven by the forces imposed on the liquid atoms at the initial stage of the S/L contact. Then the surface forces are computed by placing an Al probe atom at different positions close to the 3O-terminated (0001) sapphire surface, whose *z*-components are averaged along the *z*-direction to obtain surface force profile (Fig. 5c where the top of the sapphire surface is set as $z = 0$). By comparing Fig. 5b and Fig. 5c, we find that the surface forces are larger than the forces at the interface. This is because, when the force distribution at the sapphire surface is calculated, the probe positions are evenly distributed in each layer including many far-from-equilibrium positions. The large number of probe positions averaged within each bin along the *z*-direction ensures the result depicted in Fig. 5c to correctly describe the main features of the sapphire surface force profile. It is worth noting that only one atomic layer is predicted from Fig. 5c (shown by the horizontal dotted blue line), which is approximately at the position where the 1.6 Al layer appears when liquid Al is present. The driving forces for the formation of PNL1 and PNL2 are absent in Fig. 5c, which suggests that the PNLs are induced by the substrate–liquid Al interaction rather than the substrate alone and that the 1.6 Al layer is vital to the PNL formation.

Charge transfer and bonding features are analysed to unveil the substrate–liquid Al interaction. Planar-averaged deformation charge density profile $\Delta\rho(z)$ and electron localisation function (ELF)[37,41,42] are calculated to characterise the features of charge transfer and bonding, as shown in Fig. 5e. Deformation charge density is obtained according to the following formula:

$$\Delta\rho = \rho_{\mathrm{Tot}}^{\mathrm{sc}} - \rho_{\mathrm{Al}}^{\mathrm{atomic}} - \rho_{\mathrm{o}}^{\mathrm{atomic}} \quad (1)$$

where $\rho_{\mathrm{Tot}}^{\mathrm{sc}}$ is the self-consistent charge density and $\rho_{\mathrm{Al}}^{\mathrm{atomic}}$ and $\rho_{\mathrm{o}}^{\mathrm{atomic}}$ are the superposition of isolated atomic charge density. The positive and negative $\Delta\rho(z)$ peaks in alternating order indicate the formation of chemical bonds between two consecutive atomic layers (Fig. 5e). It is clearly shown in Fig. 5e that the 1.6 Al layer, acting as an anchor, forms chemical bonds with both the 3O and PNL1 layers by transferring electrons to the 3O layer and accepting electrons from the PNL1. The isosurface of ELF = 0.8, which exhibits the distribution of localised bonds (such as the covalent or ionic bonds), is shown in Fig. 5e. It clearly shows that the chemical bonds around the 1.6 Al layer (1.6 Al–3O and 1.6 Al–PNL1) consist of a large portion of localised bonds. These localised bonds strengthen the connection between the 1.6 Al layer and the PNL1 and maintain the relatively high degree of out-of-plane ordering. The charge transfer and the formation of the localised bonds are two characteristic features of the sapphire–liquid Al interaction, which play critical roles in the synergistic ordering of the 1.6 Al and PNL1 layers. For the PNL2, its interaction with the sapphire substrate is much weaker (minor charge transfer and a negligible portion of localised bonds) compared with the PNL1, which leads to its poorly ordered structure.

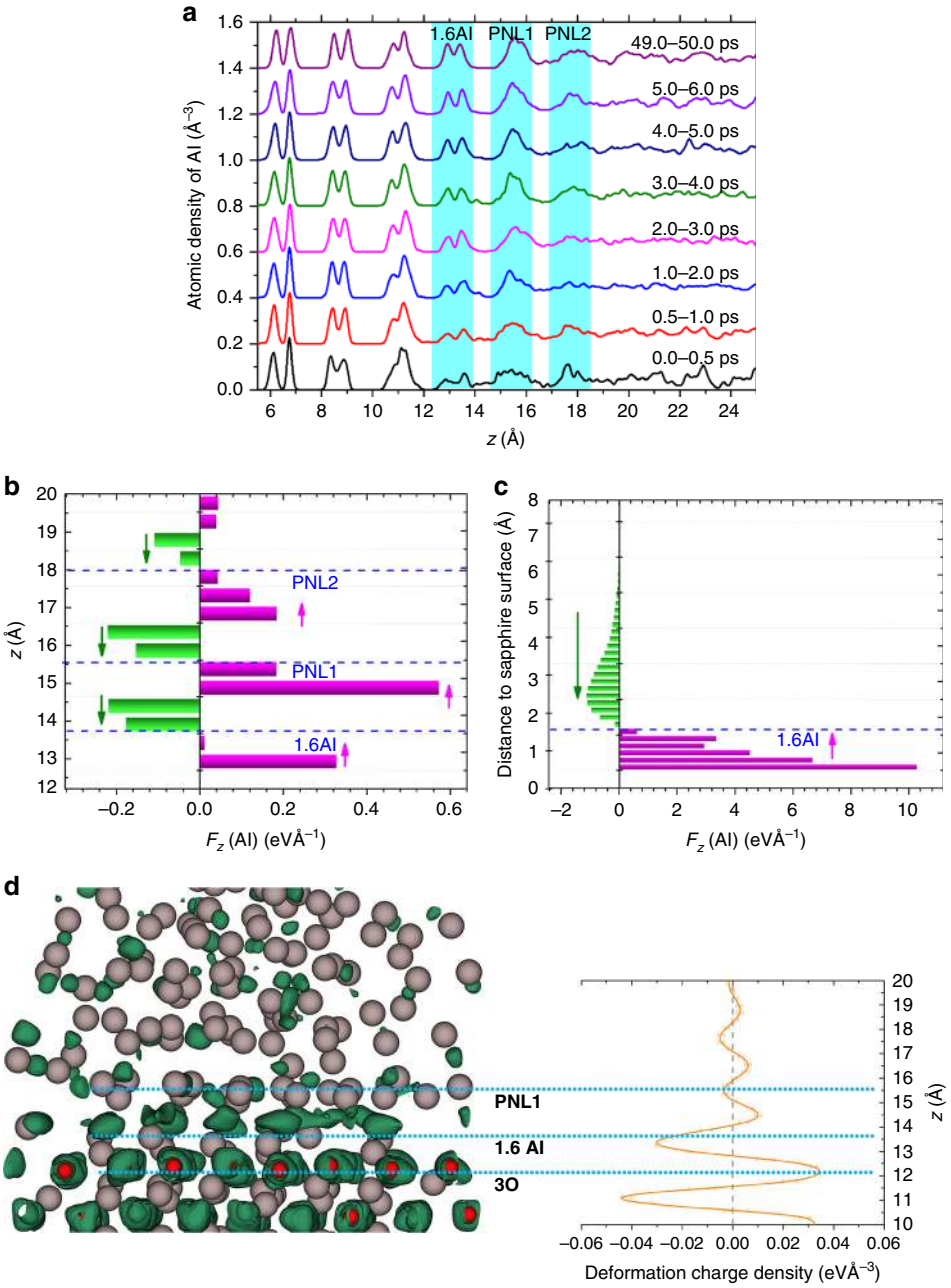


**Fig. 5** Kinetics and mechanism of pre-nucleation layering. **a** Atomic (Al atoms) density profile evolution over time, which depicts the kinetics of pre-nucleation layering. The evolution of the 1.6 Al layer, the PNL1 and the PNL2 are highlighted in the cyan regions. **b** Force profile in liquid Al at the (0001) sapphire–liquid Al interface. The horizontal dotted blue lines in **b** show the predicted positions of the atomic layers at the studied interface, which are approximately where the 1.6 Al layer, the PNL1 and the PNL2 appear, respectively. **c** Surface force profile at the 3O-terminated (0001) sapphire surface. $z = 0$ is aligned with the top of the sapphire surface. Only one atomic layer (horizontal dotted blue line in **c**) can be predicted from the surface force profile, which is close to the position where the 1.6 Al layer forms when liquid Al is present. Positive (or negative) forces imposed on Al atoms are described by the pink (or green) bars in both **b** and **c**, which drive the atoms to move away from (or toward) the interface, as shown by the pink (or green) arrows. **d** Electron localisation function (ELF) = 0.8 isosurface structure (shown by the green features in the left panel) showing the distribution of localised bonds at the interface (small red spheres are the O atoms and large grey spheres are the Al atoms); planar-averaged deformation charge density distribution (amber wave in the right panel) along the *z*-direction that depicts the charge transfer between the pre-nucleation layers (PNLs) and the sapphire substrate. The three cyan dotted horizontal lines in **d** indicate the average positions of the 1.6 Al layer, the PNL1 and the PNL2, respectively

From the above discussion, we conclude that the PNLs near the (0001) sapphire substrate are induced by the substrate–liquid Al interaction, which is manifested by the charge transfer at the interface and the formation of covalent/ionic bonds between the 1.6 Al layer and the PNLs. As a result of the substrate–liquid Al interaction, $F_z$(A1) with oscillatory profile develops in the liquid Al adjacent to the sapphire substrate leading to the appearance of the 1.6 Al layer and the PNLs. In other words, the pre-nucleation liquid layering can be described as the adsorption of liquid atoms onto the substrate, which is a spontaneous and deterministic process.

**Mechanistic insight into aluminium nucleation on sapphire surface**. In this work, the CTR curves are measured in situ to shed

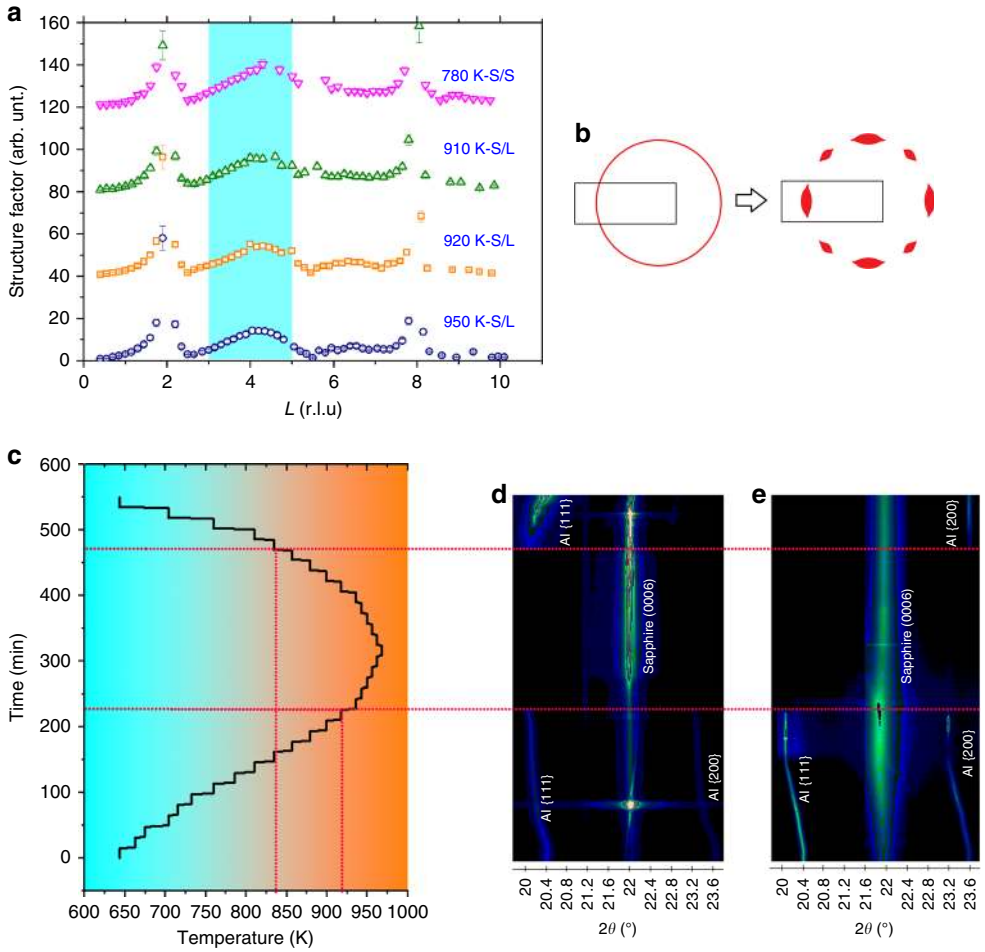


**Fig. 6** In situ CTR and in situ X-ray diffraction at the (0001) sapphire–Al interface during the heating–cooling process. **a** Evolution of the CTR curves during the Al solidification on the (0001) sapphire surface. The intensity peak at $L = 3$–5, which is a typical feature attributed to the two PNLs at the interface, is highlighted in the cyan region in **a**. No obvious change of the highlighted intensity peak can be observed, indicating that no more PNL forms during the cooling process. **b** Schematic illustration showing the transformation of Al (111) (or (200)) diffraction feature from ring-like to spot-like as a result of the coarsening of the Al grains after solidification compared with the initial deposited grain structure. **c** Heating–cooling curve. **d**, **e** Two typical in situ XRD results showing the evolution of the XRD patterns during the heating–cooling processes. A series of detector images in an entire scan are concatenated into a single stack, and **d**, **e** are the orthogonal views of such stacks. In **d**, **e**, the fluorescent (and blue) streaks show the evolution of the diffraction features of Al {111} planes, sapphire (0006) plane and Al {200} planes during the heating–cooling cycles, respectively. By monitoring the change of the diffraction features related to Al, the onset temperature melting and solidification of Al can be determined, as shown by the two red dotted lines crossing **c**–**e**. The reappearance of the diffraction features from Al {111} planes and Al {200} planes is observed in two independent heating–cooling cycles, respectively, as shown in **d**, **e**. This is a result of the coarsening of the Al grains after solidification compared with the initial deposited Al grain structure, which causes the diffraction features to transform from ring-like to spot-like (as depicted in **b**). Considering the limited size of the detector, it is reasonable that the diffraction features from the two different planes of Al were not collected in one scan. More importantly, the reappearance of both Al {111} planes and Al {200} planes supports the heterogeneous nucleation behaviour through stochastically formed nuclei rather than the continuation of liquid layering

light on the evolution of the PNLs as temperature decreases. In Fig. 6a, the CTR curves at four typical temperatures are displayed. Interestingly, all these CTR curves, including those measured after the solidification of the liquid Al, have the typical feature of the intensity peak at $L = 3$–5, which is attributed to the PNLs according to the above analysis. Therefore, the PNLs retain during the cooling process. In addition, the difference between these CTR curves is negligible; this implies that no more PNLs are triggered, because extra PNLs would significantly change the CTR curve, particularly the intensity peak at $L = 3$–5. A similar result to the above experimental phenomenon is obtained in the AIMD simulations by monitoring the liquid layering during the cooling of the (0001) sapphire–Al S/L interface. As shown in Supplementary Figure 3 and Supplementary Figure 4, no evident liquid layering occurs in the proximity of the double-layer PNLs even when an extremely large undercooling (233 K) is reached.

By the combination of in situ CTR and AIMD analysis, we unambiguously identify that the liquid layering cannot dominate the heterogeneous nucleation of crystalline Al on (0001) sapphire substrate and thus nucleation through layer-by-layer atomic adsorption is not favoured. Therefore, it is intriguing to determine how the heterogeneous nucleation of crystalline Al proceeds in the undercooled liquid Al near the (0001) sapphire surface. Even though the large undercooling cannot promote the liquid layering, it will bring the crystal embryos originating from the energy fluctuations to stable nuclei according to the CNT. Therefore, we argue that these stochastically formed nuclei dominate the heterogeneous nucleation behaviour. It is worth noting that the intermediate layer evolved from the PNLs becomes the surface structure to trigger the heterogeneous nucleation of crystalline Al, so the pre-nucleation liquid layering still plays a key role in determining the heterogeneous nucleation behaviours in this system.

The stochastically formed nuclei with arbitrary orientations tend to form non-coherent interfaces with the substrate to release the interfacial stress thus manifesting different lattice parameters from the substrate. The difference in the crystallographic characteristics between the nuclei and the sapphire substrate makes the nuclei's contribution to the CTRs (with integer Miller indices $H$ and $K$) measured in our experiments negligible. This is consistent with the in situ CTR results that no evident change of the CTR curve can be observed during the nucleation and ensuing solidification process of crystalline Al phase. Figure 6 exhibits the in situ XRD results during two independent heating–cooling processes. The initial solid Al microstructure obtained from magnetron sputtering contains both Al (111) and Al (200) peaks. Upon heating, both peaks disappear at around 225 min under around 935 K. During the cooling process, the reappearance of both the Al (111) and Al (200) peaks is observed in Fig. 6, which suggests that the Al grains with different crystal orientations form during the cooling process. This phenomenon supports the above argument that the appearance of stochastically formed nuclei dominates the heterogeneous nucleation of crystalline Al. We note that, compared with the Al microstructure obtained from magnetron sputtering, the solidified Al microstructure may have a larger grain size, which transforms the diffraction rings into several discontinuous diffraction spots[43] as shown in Fig. 6b. Consequently, for a detector with a limited size, it is reasonable to capture just one diffraction peak from the solidified Al. In summary, both the in situ CTR and in situ XRD results support the heterogeneous nucleation mechanism proposed above.

**Thermodynamic analysis of pre-nucleation liquid layering.** Revealing the mechanism of pre-nucleation liquid layering is a long-standing issue[8,9,44–49]. In the following, we will analyse the liquid layering in the perspective of interfacial thermodynamics. As schematically presented in Fig. 7b, an S/L interface with PNLs can be divided into three regions along the $z$-direction: (1) region of the solid substrate (S), (2) region of the PNLs (PNL), and (3) region of the bulk liquid (L). As a reference, the initial S/L interface without the PNLs is also shown in Fig. 7a. The total energy ($E_{\mathrm{inter}}$) of an interface system can be expressed as the sum of volumetric Gibbs free energy ($G_{\mathrm{v}}$), elastic strain energy ($E_{\mathrm{strain}}$) and interfacial free energy ($\gamma$). Additionally, we note that the degree of ordering for the quasi-layers in the PNL region decays with distance to the substrate increasing. Hence, an extra gradient energy ($\phi$) due to the inhomogeneous feature of the PNL region is also expected to contribute to the total energy. The total energy of the initial interface (Fig. 7a) has the following formula:

$$E_{\mathrm{inter}}^{\mathrm{initial}} = g_{\mathrm{vS}} \cdot A \cdot W_{\mathrm{S}} + g_{\mathrm{vL}} \cdot A \cdot W_{\mathrm{L}} + g_{\mathrm{vL}} \cdot A \cdot W_{\mathrm{PNL}} + \gamma_{\mathrm{S/L}} \cdot A \quad (2)$$

where $g_{\mathrm{vS}}$ and $g_{\mathrm{vL}}$ are the volumetric Gibbs free energy per unit volume for the substrate and liquid regions, respectively; $A$ denotes the interfacial area; $W_{\mathrm{S}}$, $W_{\mathrm{L}}$ and $W_{\mathrm{PNL}}$ are the thickness of substrate, liquid and PNL regions, respectively, as shown in Fig. 7; and $\gamma_{\mathrm{S/L}}$ indicates the interfacial free energy of the S/L interface as shown in Fig. 7a. Then the total energy of the interface with the PNLs is expressed as follows:

$$E_{\mathrm{inter}}^{\mathrm{layering}} = g_{\mathrm{vS}} \cdot A \cdot W_{\mathrm{S}} + g_{\mathrm{vL}} \cdot A \cdot W_{\mathrm{L}} + (g_{\mathrm{vPNL}}^{\mathrm{layering}} + \varphi^{\mathrm{layering}} + e_{\mathrm{strain}}^{\mathrm{layering}}) \cdot A \cdot W_{\mathrm{PNL}} + (\gamma_{\mathrm{PNL/S}} + \gamma_{\mathrm{PNL/L}}) \cdot A \quad (3)$$

In this formula, $\varphi^{\mathrm{layering}}$ and $e_{\mathrm{strain}}^{\mathrm{layering}}$ are the gradient energy and elastic energy per unit volume in the PNLs and $\gamma_{\mathrm{PNL/S}}$ and $\gamma_{\mathrm{PNL/L}}$ denote the interfacial free energy of the PNL/S and PNL/L interfaces, respectively.

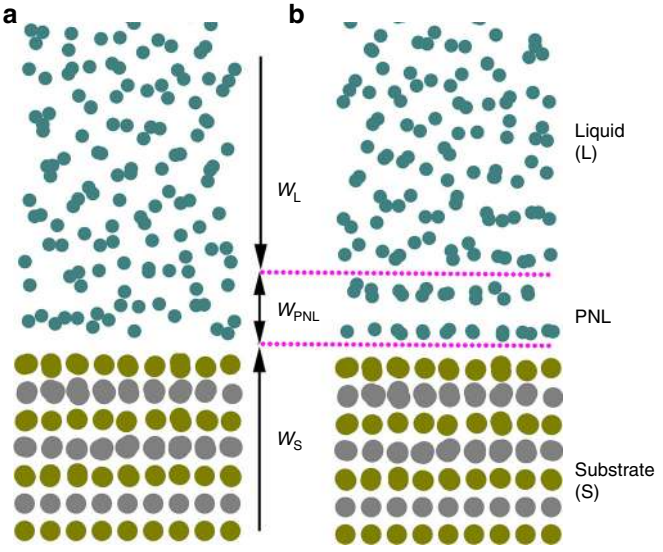


**Fig. 7** Schematic illustration of the three-region model used in the interfacial thermodynamics analysis to reveal the liquid layering mechanism. **a** The initial interface model without the PNLs. **b** The evolved interface model with the PNLs, which can be divided into three regions (by the horizontal dotted pink lines): the substrate region, the PNL region, and the liquid region. The widths of these three regions are denoted as $W_s$, $W_{\mathrm{PNL}}$ and $W_{\mathrm{L}}$, respectively, as shown by the arrows in the figure. The green, yellow and grey dots in this figure are used to schematically represent three different atom types

Energy change due to the liquid layering can be readily obtained by subtracting $E_{\mathrm{inter}}^{\mathrm{initial}}$ from $E_{\mathrm{inter}}^{\mathrm{layering}}$:

$$\Delta E_{\mathrm{inter}}^{\mathrm{layering}} = (g_{\mathrm{vPNL}}^{\mathrm{layering}} - g_{\mathrm{vL}} + \varphi^{\mathrm{layering}} + e_{\mathrm{strain}}^{\mathrm{layering}}) \cdot A \cdot W_{\mathrm{PNL}} + (\gamma_{\mathrm{PNL/S}} + \gamma_{\mathrm{PNL/L}} - \gamma_{\mathrm{S/L}}) \cdot A \quad (4)$$

PNLs normally appear when the temperature is above $T_1$. In this temperature range, the disordered liquid phase has the lowest volumetric Gibbs free energy. Pre-nucleation liquid layering increases the crystallinity, which reduces the liquid phase entropy thus increasing the volumetric Gibbs free energy, i.e. $g_{\mathrm{vPNL}}^{\mathrm{layering}} - g_{\mathrm{vL}} > 0$. Therefore, the volume-related parameters ($g$, $\varphi$ and $e$) are the barriers for the pre-nucleation liquid layering. Consequently, the area-related term in Eq. (4) (or the interfacial free energy reduction $\Delta\gamma = \gamma_{\mathrm{PNL/S}} + \gamma_{\mathrm{PNL/L}} - \gamma_{\mathrm{S/L}}$) becomes the only possible driving force for the PNL formation.

The S/L interfacial energy reduction $\Delta\gamma$ can be reflected in the transitions of the valence charge density and the electrostatic potential energy across the interface, as shown in Fig. 8. In the sapphire substrate, the profiles of valence charge density and electrostatic potential energy along the $z$-direction are strongly oscillatory with valence electrons localised around the O atoms, while in the bulk liquid Al, the profiles are nearly constant, as expected for metallic bonds. The substrate–-liquid Al interaction causes electrons to transfer from the liquid Al to the 1.6 Al layer of the sapphire substrate. Consequently, the (0001) sapphire surface becomes negatively charged. Then near this negatively charged surface, oscillatory charge density occurs with positive and negative charges arranging in alternating order (Fig. 8c). This phenomenon is quite similar to the Friedel oscillations[50] (or quantum oscillations[51]), which are beneficial to the energy optimisation of the systems. As a result, the electrostatic potential energy is induced to be oscillatory along the $z$-direction as shown in Fig. 8c, which can be regarded as a continuation of that from the bulk sapphire.

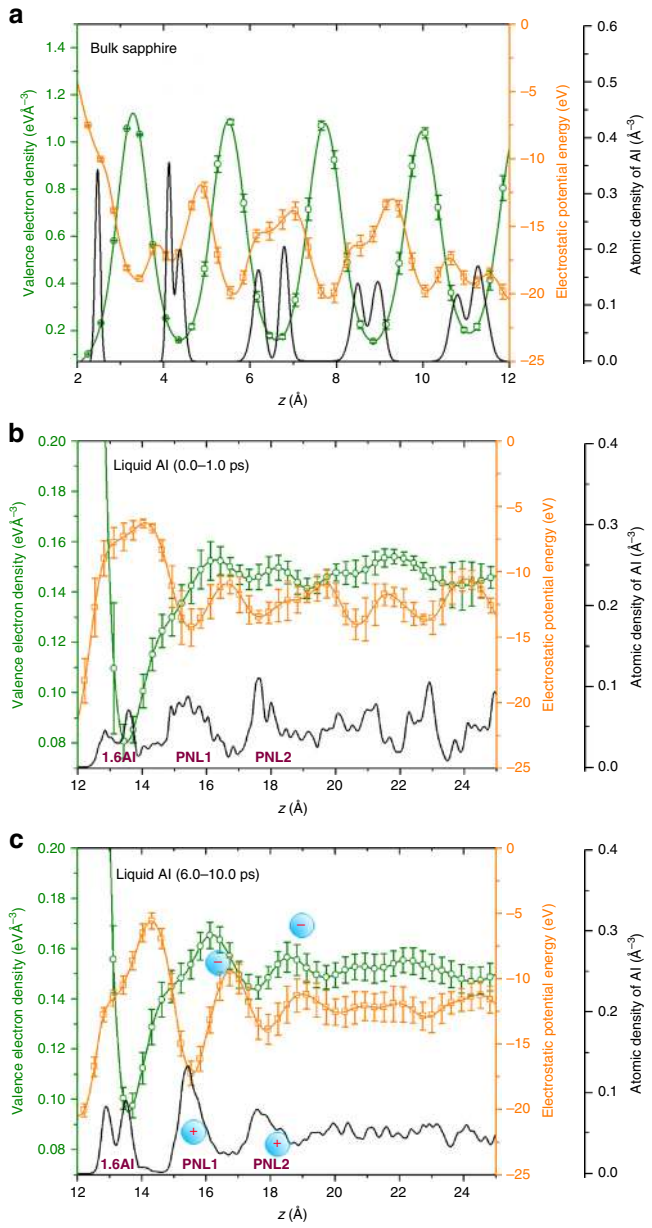


**Fig. 8** Valence charge density and electrostatic potential energy profiles across the (0001) sapphire–liquid Al interface. **a** Planar-averaged valence charge density, planar-averaged electrostatic potential energy and atomic (Al atoms) density profile along the *z*-direction in the bulk sapphire. **b**, **c** The profiles of the above three parameters across the interface averaged over 0.0–1.0 ps (without the 1.6 Al layer and PNLs) and over 6.0–10.0 ps (with the 1.6 Al layer and the PNLs), respectively. The positions of the 1.6 Al layer, the PNL1 and the PNL2 are shown in **b** and **c**, respectively. Substrate–liquid Al interaction causes electrons to transfer from the liquid Al to the 1.6 Al layer of the sapphire substrate resulting in a negatively charged sapphire surface. This negatively charged surface triggers oscillatory charge density with positive and negative charges arranging in alternating order (as schematically illustrated by the blue circles with + or − charge symbols). Consequently, the electrostatic potential energy is induced to be oscillatory along the *z*-direction. These phenomena are believed to be connected with the interfacial energy reduction, which is the driving force for the pre-nucleation liquid layering. The profiles in this figure are obtained by averaging the valence charge densities or electrostatic potential energies along the AIMD trajectory with error bars being the standard deviations

Compared with the initial abrupt transition across the interface, the oscillatory electrostatic potential energy profile makes the interfacial transition 'smoother' and more symmetrical and thus reduces the electrostatic contribution to the interfacial energy. Therefore, we believe this Friedel-oscillation-like phenomenon observed at the (0001) sapphire–liquid Al interface can effectively reduce the interfacial energy, which is the underlying reason for the occurrence of pre-nucleation liquid layering.

## Discussion

According to the above thermodynamic analysis, we demonstrate that the interfacial energy reduction $\Delta\gamma$ provides the driving force for the pre-nucleation liquid layering; however, this process is hindered mainly by the interfacial strain energy that arises from the lattice mismatch between the substrate and the partly ordered PNL structure. Based this analysis, the poorly ordered in-plane structure of the PNLs at the (0001) sapphire–liquid Al interface is readily understood that $\Delta\gamma$ is not sufficiently large to surmount the interfacial strain energy barrier caused by the formation of the PNLs with highly ordered in-plane structure. In fact, the degree of ordering of the PNL1 is critical to the further liquid layering process. In this study, we show that the in-plane structure of the PNL1 remains poorly ordered even when a large undercooling (233 K) is reached. As a result, it is difficult for the liquid layering to proceed. Accordingly, we propose that nuclei caused by the energy fluctuations may appear stochastically at the surface of the PNLs when undercooling is large enough, which is supported by the in-situ CTR and XRD experimental results. Therefore, the evolution of the (0001) sapphire–Al interface structure is summarised as follows: (1) when the liquid Al is brought into contact with the sapphire substrate at a temperature higher than $T_1$, the 1.6 Al layer and the double-layer PNLs appear; (2) after the temperature falls below $T_1$, the liquid layering competes with the energy fluctuations to control the heterogeneous nucleation behaviour, and at the studied interface in this work, the energy fluctuations dominate and heterogeneous nucleation is controlled by the stochastic formation of the nuclei at the PNL surface. In summary, the pre-nucleation liquid layering is mainly determined by the competition between the interfacial energy reduction $\Delta\gamma$ and the interfacial strain energy barrier and then the heterogeneous nucleation behaviour is dominated by the competition between the liquid layering and the stochastic formation of the nuclei due to the energy fluctuations in the liquid Al.

## Methods

**Sample**. Single-crystal sapphire substrates with the (0001) surface are provided by Shanghai Institute of Optics and Fine Mechanics. The surface roughness of these substrates is tested to be within nanometre scale (Supplementary Figure 5c) by atomic force microscopy, and only Al and O elements are detectable on the surfaces by energy dispersive X-ray spectroscopy. To prepare the (0001) sapphire–Al interface samples, magnetron sputtering is employed to deposit a 1-μm-thick Al overlayer on the sapphire substrate. The Al overlayer thickness has been determined[22] to be suitable for providing sufficient material to hold the liquid region in a reasonable shape upon melting, while ensuring enough X-ray beam penetration through the Al layer into the bulk sapphire substrate.

**CTR scattering measurement and analysis**. The experimental set-up is schematically shown in Supplementary Figure 5. The samples are placed into an ultra-high vacuum chamber in all experiments. X-rays of 15 KeV with an illuminated area of $0.25 \times 0.2\ mm^2$ are used in the Diamond Light Source beamline I07. CTRs of the (0001) sapphire surface and the interface between (0001) sapphire and the deposited Al are first collected at room temperature. Then, to explore the evolution of the (0001) sapphire–Al interface during the Al melting and solidification process, particularly the structural properties of the S/L interface, the sample with the deposited Al overlayer undergoes several heating–cooling cycles during which CTRs are extracted in situ. In situ XRD patterns are also recorded during the heating–cooling cycles to determine the temperature range in which the Al overlayer is in a liquid state. This has been discussed in detail in our previous work[22]. The collected intensity $I_{HKL}$ of the CTRs is corrected for effective sample area, the polarisation of the X-ray beam and the Lorentz

factor and then transformed into the structure factor $F_{HKL}$ through $F_{HKL} = \sqrt{I'_{HKL}}$ ($I'_{HKL}$ is the corrected intensity) before fitting. The estimated experimental data error is derived from the statistical uncertainty of the measured intensity and is set to 10% whenever it is <10%, which is an estimate of the systematic error[27].

CTR fitting is conducted using the ROD software[34]. During the fitting, the atomic coordinates and the atomic occupancies are used as fitting parameters, which are the essential parameters in determining the surface/interface structures. The DW parameters, which quantify the influence of temperature on the diffraction, are also used as fitting parameters. Besides, the surface roughness is characterised using the approximate $\beta$ model[52]. The small value of the fitted surface roughness parameter ($\beta = 0.04 \pm 0.006$ obtained by fitting the (01$L$) CTR) is consistent with the nanometre-scale surface roughness of the sapphire substrates used in the experiment (Supplementary Figure 5c).

**AIMD calculation**. AIMD is performed using Vienna ab initio simulation package[53,54]. Ion cores are treated using projector-augmented waves[55,56] method with the cut-off energy of 400 eV. Exchange-correlation energy is described by the generalised gradient approximation of Perdew–Burke–Ernzerhof[57], which proves to be more accurate and closer to experimental results for the sapphire systems[37,58]. Mixed block Davidson iteration with residual minimisation using direct inversion in the iterative subspace and Gaussian smearing method with a smearing width of 0.01 eV are applied to obtain the ground-state charge density.

For molecular dynamics, canonical (*NVT*) ensemble is used with a time step of 1.0 fs. Nosé thermostat is employed to keep the temperature of the simulated system around 950 K, which is just above the melting points of the AIMD model of Al[59,60]. The initial S/L interfacial structure is prepared using the approach proposed by Wang et al.[61] by combining a $(3 \times 3)$ (0001) sapphire substrate (15 layers) with an equilibrated liquid Al sample obtained from the simulation in LAMMPS[62] using the Embedded-Atom model potential[63]. Larger supercell size $(4 \times 4)$ has also been tested, which shows a statistically insignificant difference compared to the $(3 \times 3)$ supercell used in this work (Supplementary Figure 6). The interface is oriented normal to the $z$ axis. A total of 417 atoms are contained in the model, so only the $\Gamma$-point is used to sample the Brillouin zone. AIMD simulation runs for 50.0 ps, during which atomic density profile along the $z$-direction[39] is recorded to characterise the layering feature; the orientation order parameter[39], the in-plane coordination number $N_{in}$ and the 2D structural factor distribution are calculated to describe the in-plane structure.

Atomic density profile is computed using the following formula:

$$\rho(z) = \frac{<n_z>}{A_{xy}\Delta z} \quad (5)$$

where $<n_z>$ is the time-averaged number of atoms in the bin between $z-\Delta z/2$ and $z+\Delta z/2$; $A_{xy}\Delta z$ is the volume of the bin. Orientation order parameter $q_n$ is calculated according to the following formula:

$$q_n = \frac{<\sum_{i,j,k}\cos[n\theta_{xy}(m,a,b)]>}{N_{\cos}} \quad (6)$$

where $n$ is an integer; $m$, $a$ and $b$ denote three atoms within the same liquid layer with $a$ and $b$ being the nearest neighbours of $m$; and $\theta_{xy}(m, a, b)$ is the angle between $\mathbf{r_{ma}}$ and $\mathbf{r_{mb}}$ projected on the $xy$ plane. $N_{\cos}$ is the number of cos[] added in a time step. $q_6$ is studied here as it varies from nearly 0 for a totally disordered liquid to 1 for a perfect close-packed atomic layer (such as the (111) layer in an FCC crystal)[39]. $N_{in}$ is calculated by counting for each atom the number of nearest neighbour atoms within the cut-off radius $r_{cut} = 3.5$ Å and then averaging within each bin. 2D structure factor distribution $s(\mathbf{q})$ is calculated as follows:

$$s(\mathbf{q}) = \frac{1}{N}<\sum_{a=1}^{N}\sum_{b=1}^{N} e^{-i\mathbf{q}\cdot(\mathbf{r_a}-\mathbf{r_b})}> = \frac{1}{N}<\left|\sum_{a=1}^{N}\cos(\mathbf{q}\cdot\mathbf{r_a})\right|^2 + \left|\sum_{b=1}^{N}\sin(\mathbf{q}\cdot\mathbf{r_b})\right|^2> \quad (7)$$

where $\mathbf{q}$ is the scattering vector, which is a vector in the reciprocal space; $N$ is the number of atoms in a liquid layer; $i$ denotes an imaginary unit; and $\mathbf{r_a}$ and $\mathbf{r_b}$ are the positions of atom $a$ and atom $b$, respectively.

## Data availability

The data sets that support the findings of the current study are available from the corresponding author on reasonable request.

Received: 20 July 2018 Accepted: 26 November 2018
Published online: 04 January 2019

## References

1. Kelton, K. & Greer, A. L. *Nucleation in Condensed Matter: Applications in Materials and Biology* (Elsevier, Oxford, 2010).
2. Russo, J. & Tanaka, H. Crystal nucleation as the ordering of multiple order parameters. *J. Chem. Phys.* **145**, 211801 (2016).
3. Huisman, W. J. et al. Layering of a liquid metal in contact with a hard wall. *Nature* **390**, 379–381 (1997).
4. Oh, S. H., Kauffmann, Y., Scheu, C., Kaplan, W. D. & Rühle, M. Ordered liquid aluminum at the interface with sapphire. *Science* **310**, 661–663 (2005).
5. Reichert, H., Denk, M., Okasinski, J., Honkimäki, V. & Dosch, H. Giant metal compression at liquid-solid (Pb-Si, In-Si) Schottky junctions. *Phys. Rev. Lett.* **98**, 116101 (2007).
6. Schülli, T. et al. Substrate-enhanced supercooling in AuSi eutectic droplets. *Nature* **464**, 1174–1777 (2010).
7. Gandman, M., Kauffmann, Y., Koch, C. T. & Kaplan, W. D. Direct quantification of ordering at a solid-liquid interface using aberration corrected transmission electron microscopy. *Phys. Rev. Lett.* **110**, 086106 (2013).
8. Comtet, J. et al. Nanoscale capillary freezing of ionic liquids confined between metallic interfaces and the role of electronic screening. *Nat. Mater.* **16**, 634–639 (2017).
9. Duan, Y. et al. Density dependent structural phase transition for confined copper: origin of the layering. *Phys. Chem. Chem. Phys.* **20**, 9337–9342 (2018).
10. Men, H. & Fan, Z. Prenucleation induced by crystalline substrates. *Metall. Mater. Trans. A* **49**, 2766–2777 (2018).
11. Greer, A., Bunn, A., Tronche, A., Evans, P. & Bristow, D. Modelling of inoculation of metallic melts: application to grain refinement of aluminium by Al–Ti–B. *Acta Mater.* **48**, 2823–2835 (2000).
12. Quested, T. & Greer, A. The effect of the size distribution of inoculant particles on as-cast grain size in aluminium alloys. *Acta Mater.* **52**, 3859–3868 (2004).
13. Liotti, E. et al. Crystal nucleation in metallic alloys using x-ray radiography and machine learning. *Sci. Adv.* **4**, eaar4004 (2018).
14. Fan, Z. et al. Grain refining mechanism in the Al/Al–Ti–B system. *Acta Mater.* **84**, 292–304 (2015).
15. Cantor, B. Heterogeneous nucleation and adsorption. *Philos. Trans. A Math. Phys. Eng. Sci.* **361**, 409–417 (2003).
16. Ma, Z., Belyakov, S., Sweatman, K., Nishimura, T. & Gourlay, C. Harnessing heterogeneous nucleation to control tin orientations in electronic interconnections. *Nat. Commun.* **8**, 1916 (2017).
17. Wang, L. et al. Interfacial tuning for the nucleation of liquid AlCu alloy. *Acta Mater.* **139**, 75–85 (2017).
18. Greer, A. L. Liquid metals: supercool order. *Nat. Mater.* **5**, 13 (2006).
19. Kauffmann, Y. et al. Quantitative analysis of layering and in-plane structural ordering at an alumina–aluminum solid–liquid interface. *Acta Mater.* **59**, 4378–4386 (2011).
20. Kang, J. et al. Atomically abrupt liquid-oxide interface stabilized by self-regulated interfacial defects: The case of Al/$Al_2O_3$ interfaces. *Phys. Rev. Lett.* **108**, 226105 (2012).
21. Zhang, Q. et al. Adhesion and nonwetting-wetting transition in the Al/α−$Al_2O_3$ interface. *Phys. Rev. B* **69**, 045423 (2004).
22. Brown, A., Dong, H., Howes, P. & Nicklin, C. In situ observation of the orientation relationship at the interface plane between substrate and nucleus using X-ray scattering techniques. *Scr. Mater.* **77**, 60–63 (2014).
23. Kaplan, W. D. & Kauffmann, Y. Structural order in liquids induced by interfaces with crystals. *Annu. Rev. Mater. Res.* **36**, 1–48 (2006).
24. Kaplan, W. D., Chatain, D., Wynblatt, P. & Carter, W. C. A review of wetting versus adsorption, complexions, and related phenomena: the rosetta stone of wetting. *J. Mater. Sci.* **48**, 5681–5717 (2013).
25. Gustafson, J., et al. High-energy surface X-ray diffraction for fast surface structure determination. *Science* **343**, 758–761 (2014).
26. Nicklin, C. Capturing Surface Processes. *Science* **343**, 739–740 (2014).
27. Charlton, G. et al. Relaxation of $TiO_2$ (110)-(1×1) using surface X-ray diffraction. *Phys. Rev. Lett.* **78**, 495 (1997).
28. Eng, P. J. et al. Structure of the hydrated α-$Al_2O_3$ (0001). *Surf. Sci.* **288**, 1029–1033 (2000).
29. Morisaki, H. et al. Large surface relaxation in the organic semiconductor tetracene. *Nat. Commun.* **5**, 5400 (2014).
30. Vonk, V., Cremers, M., de Jong, A., Pintea, S. & Vlieg, E. Atomic layering and misfit-induced densification at the Si (111)/In solid–liquid interface. *Surf. Sci.* **621**, 69–76 (2014).
31. Dupraz, M. et al. Wetting layer of copper on the tantalum (001) surface. *Phys. Rev. B* **94**, 235427 (2016).
32. Liu, Y., Kawaguchi, T., Pierce, M. S., Komanicky, V. & You, H. Layering and ordering in electrochemical double layers. *J. Phys. Chem. Lett.* **9**, 1265–1271 (2018).
33. Bracco, J. N. et al. Hydration structure of the barite (001)–water interface: Comparison of x-ray reflectivity with molecular dynamics simulations. *J. Phys. Chem. C* **121**, 12236–12248 (2017).
34. Vlieg, E. ROD: a program for surface X-ray crystallography. *J. Appl. Crystallogr.* **33**, 401–405 (2000).
35. Wang, X.-G., Chaka, A. & Scheffler, M. Effect of the environment on α−$Al_2O_3$ (0001) surface structures. *Phys. Rev. Lett.* **84**, 3650 (2000).

36. Łodziana, Z. & Nørskov, J. K. Adsorption of Cu and Pd on α-$Al_2O_3$ (0001) surfaces with different stoichiometries. *J. Chem. Phys.* **115**, 11261–11267 (2001).
37. Siegel, D. J., Hector, L. G. & Adams, J. B. Adhesion, atomic structure, and bonding at the Al (111)/α−$Al2_O3$ (0001) interface: a first principles study. *Phys. Rev. B* **65**, 085415 (2002).
38. Han, Y., Dai, Y., Shu, D., Wang, J. & Sun, B. First-principles calculations on the stability of Al/$TiB_2$ interface. *Appl. Phys. Lett.* **89**, 144107 (2006).
39. Davidchack, R. L. & Laird, B. B. Simulation of the hard-sphere crystal–melt interface. *J. Chem. Phys.* **108**, 9452–9462 (1998).
40. Alert, R., Casademunt, J. & Tierno, P. Landscape-inversion phase transition in dipolar colloids: tuning the structure and dynamics of 2D crystals. *Phys. Rev. Lett.* **113**, 198301 (2014).
41. Becke, A. D. & Edgecombe, K. E. A simple measure of electron localization in atomic and molecular systems. *J. Chem. Phys.* **92**, 5397–5403 (1990).
42. Jarvis, E. A. & Carter, E. A. Metallic Character of the $Al_2O_3$ (0001)-($\sqrt{31}\times\sqrt{31}$) R ± 9° Surface Reconstruction. *J. Phys. Chem. B* **105**, 4045–4052 (2001).
43. Iqbal, N. et al. Real-time observation of grain nucleation and growth during solidification of aluminium alloys. *Acta Mater.* **53**, 2875–2880 (2005).
44. Dijkstra, M. Capillary freezing or complete wetting of hard spheres in a planar hard slit? *Phys. Rev. Lett.* **93**, 108303 (2004).
45. Walker, B. G., Marzari, N. & Molteni, C. Ab initio studies of layering behavior of liquid sodium surfaces and interfaces. *J. Chem. Phys.* **124**, 174702 (2006).
46. Laird, B. B. & Davidchack, R. L. Wall-induced prefreezing in hard spheres: a thermodynamic perspective. *J. Phys. Chem. C.* **111**, 15952–15956 (2007).
47. Page, A. & Sear, R. Freezing in the bulk controlled by prefreezing at a surface. *Phys. Rev. E* **80**, 031605 (2009).
48. Zhang, H. et al. Wall-induced phase transition controlled by layering freezing. *Phys. Rev. E* **89**, 032412 (2014).
49. Alba-Simionesco, C. et al. Effects of confinement on freezing and melting. *J. Phys. Condens. Matter* **18**, R15 (2006).
50. Friedel, J. XIV. The distribution of electrons round impurities in monovalent metals. *Lond. Edinb. Dubl. Philos. Mag.* **43**, 153–189 (1952).
51. Kohn, W. & Sham, L. Quantum density oscillations in an inhomogeneous electron gas. *Phys. Rev.* **137**, A1697 (1965).
52. Robinson, I. K. Crystal truncation rods and surface roughness. *Phys. Rev. B* **33**, 3830 (1986).
53. Kresse, G. & Hafner, J. Ab initio molecular-dynamics simulation of the liquid-metal–amorphous-semiconductor transition in germanium. *Phys. Rev. B* **49**, 14251 (1994).
54. Kresse, G. & Furthmuller, J. Efficient iterative schemes for ab initio total-energy calculations using a plane-wave basis set. *Phys. Rev. B* **54**, 11169–11186 (1996).
55. Kresse, G. & Joubert, D. From ultrasoft pseudopotentials to the projector augmented-wave method. *Phys. Rev. B* **59**, 1758–1775 (1999).
56. Blöchl, P. E. Projector augmented-wave method. *Phys. Rev. B* **50**, 17953–17979 (1994).
57. Perdew, J. P., Burke, K. & Ernzerhof, M. Generalized gradient approximation made simple. *Phys. Rev. Lett.* **77**, 3865 (1996).
58. Liu, Y. & Ning, X.-S. Influence of α-$Al_2O_3$ (0001) surface reconstruction on wettability of Al/$Al_2O_3$ interface: a first-principle study. *Comput. Mater. Sci.* **85**, 193–199 (2014).
59. Alfe, D. First-principles simulations of direct coexistence of solid and liquid aluminum. *Phys. Rev. B* **68**, 064423 (2003).
60. Bouchet, J., Bottin, F., Jomard, G. & Zérah, G. Melting curve of aluminum up to 300 GPa obtained through ab initio molecular dynamics simulations. *Phys. Rev. B* **80**, 094102 (2009).
61. Wang, J., Horsfield, A., Schwingenschlögl, U. & Lee, P. D. Heterogeneous nucleation of solid Al from the melt by TiB2 and Al3Ti: an ab initio molecular dynamics study. *Phys. Rev. B* **82**, 184203 (2010).
62. Plimpton, S. Fast parallel algorithms for short-range molecular dynamics. *J. Comput. Phys.* **117**, 1–19 (1995).
63. Mishin, Y., Farkas, D., Mehl, M. & Papaconstantopoulos, D. Interatomic potentials for monoatomic metals from experimental data and ab initio calculations. *Phys. Rev. B* **59**, 3393 (1999).


## Acknowledgements

This research was funded by the National Natural Science Foundation of China (grant numbers 51320105003 and 51674153). This research used the ALICE High Performance Computing Facility at the University of Leicester and the supercomputing facilities of National Laboratory for Information Science and Technology at Tsinghua University. S. D.M gratefully acknowledges the China Scholarship Council (CSC) for financial support. The authors acknowledge support from the Diamond Light Source for the provision of beam time (SI12083 and SI6663).

## Author contributions

S.M., A.J.B., H.D., T.J. and Q.Z. conceived and designed the project. S.M., A.J.B., H.D and R.Y. conducted most of the experiments. P.B.H., H. D. and C.N. contributed to CTR data collection and analysis. S.M., H.D. and R.L.D. performed and analysed the simulations. All authors discussed the results and collectively revised the manuscript.

## Additional information

**Supplementary information** accompanies this paper at https://doi.org/10.1038/s42004-018-0104-1.

**Competing interests:** The authors declare no competing interests.

**Reprints and permission** information is available online at http://npg.nature.com/reprintsandpermissions/

**Publisher's note:** Springer Nature remains neutral with regard to jurisdictional claims in published maps and institutional affiliations.